Anharmonicity and atomic distribution of SnTe and PbTe thermoelectrics

C. W. Li,[1,*] J. Ma,[2] H. B. Cao,[2] A. F. May,[1] D. L. Abernathy,[2] G. Ehlers,[2] C. Hoffmann,[3] X. Wang,[3] T. Hong,[2] A. Huq,[3] O. Gourdon,[4] and O. Delaire[1]

[1]*Materials Science and Technology Division, Oak Ridge National Laboratory, Oak Ridge, Tennessee 37831, USA*
[2]*Quantum Condensed Matter Division, Oak Ridge National Laboratory, Oak Ridge, Tennessee 37831, USA*
[3]*Chemical and Engineering Materials Division, Oak Ridge National Laboratory, Oak Ridge, Tennessee 37831, USA*
[4]*Lujan Center, Los Alamos National Laboratory, Los Alamos, New Mexico 87545, USA*

(Received 15 September 2014; revised manuscript received 8 December 2014; published 29 December 2014)

The structure and lattice dynamics of rock-salt thermoelectric materials SnTe and PbTe are investigated with single-crystal and powder neutron diffraction, inelastic neutron scattering (INS), and first-principles simulations. Our first-principles calculations of the radial distribution function in both SnTe and PbTe show a clear asymmetry in the first nearest-neighbor (1NN) peak, which increases with temperature, in agreement with recent experimental reports. We show that this peak asymmetry for the 1NN Sn-Te or Pb-Te bond results from large-amplitude anharmonic vibrations (phonons). No atomic off centering is found in our simulations. In addition, the atomic mean-square displacements derived from our diffraction data reveal stiffer bonding at the anion site, in good agreement with the partial phonon densities of states from INS and first-principles calculations. These results provide clear evidence for large-amplitude anharmonic phonons associated with the resonant bonding leading to the ferroelectric instability.

DOI: 10.1103/PhysRevB.90.214303 PACS number(s): 63.20.−e, 78.70.Nx

I. INTRODUCTION

Understanding phonon dynamics is very important in improving the thermoelectric efficiency. The figure of merit for thermoelectric conversion efficiency zT can be expressed as $zT = \sigma S^2 T/\kappa$, where S, T, σ, and κ are the Seebeck coefficient, temperature, electrical, and thermal conductivities, respectively. Thus, a low thermal conductivity is favorable for good thermoelectric performance. The rock-salt compounds PbTe and SnTe are particularly interesting with zT values reaching well above unity, in part thanks to the low lattice thermal conductivities $\kappa_{\rm lat} \simeq 2$ W m^{-1} K^{-1} at 300 K in single crystals [1–7]. Several factors contribute to this low $\kappa_{\rm lat}$, including soft bonds, heavy atomic masses, and strong anharmonicity, which is reflected in the proximity to a ferroelectric lattice instability [8–14].

The half-filled resonant p band and the nonlinear Te polarizability in group-IV tellurides induce a strong anharmonicity in long-range interatomic potentials [10,11,14–19]. These interactions along the [100] crystallographic directions cause the transverse-optic (TO) phonon branch to dip to low energy at the zone center. The strong anharmonicity causes this zone-center TO phonon to stiffen markedly as T increases in the cubic paraelectric phase in a clear departure from a quasiharmonic lattice [8,20–24] but in general agreement with the soft-mode picture of the ferroelectric transition [25,26].

Recently, an asymmetry of peaks was reported in the pair-distribution function (PDF) or radial-distribution function (RDF) of PbTe, PbS, and SnTe, which was interpreted in terms of atomic off centerings increasing with temperature [9,27–29]. However, it is important to note that these x-ray PDF/RDF measurements did not filter out the phonon contribution to the scattered intensity or thermal diffusive scattering. In addition, the interpretation of PDF/RDF asymmetry in terms of atomic off centerings was put in question by molecular dynamics (MD) simulations, which reproduced the asymmetry in the measurements but found no time-averaged off centering on a time scale of 12 ps or longer [11,30]. In addition, measurements of the local structure with x-ray absorption fine structure found no off centerings in PbTe [31,32]. More recently, a high-resolution neutron powder diffraction study showed no evidence for anomalies in the temperature dependence of atomic displacement parameters (ADPs) in PbS and attributed the unusual temperature behaviors reported in Refs. [27,28] for inaccurate thermometry [33].

The spectra of PbTe exhibits a broad and split peak at the zone center in the temperatures between 200 and 500 K [8,9], clearly different from a damped harmonic-oscillator profile [34]. A similar double-peak feature was also observed in frequency-dependent reflectivity measurements [35]. It had been previously conjectured that this anomaly could be related to proposed atomic off centerings causing an additional localized optical mode, beyond the dispersions of the rock-salt structure [9,27]. However, our first-principles calculations of the temperature-dependent spectral density functions showed how the double peak arises from the shape of the anharmonic phonon self-energy, whose imaginary part contains a pronounced peak, owing to nesting of the phonon dispersions [36]. Calculations of the zone-center TO phonon spectral function at the zone center in PbTe based on molecular dynamics also reproduced the effect [30,37]. Our measurements and calculations found a less unusual spectral function for the TO mode in SnTe, although its linewidth is also quite broad [36].

Whereas PbTe is an incipient ferroelectric material, intrinsic SnTe undergoes a displacive ferroelectric phase transition from a high-temperature paraelectric rock-salt phase to a rhombohedrally distorted ferroelectric phase at a Curie temperature $T_C \lesssim 100$ K with softening of the TO mode [26]. However, T_C in SnTe is strongly dependent on the introduction of extrinsic carriers, which arises from a slight off stoichiometry [21]. Samples of SnTe synthesized by a solid-state reaction are commonly found to exhibit a small Sn deficiency, owing to

*lic2@ornl.gov

slightly incongruent melting of the rock-salt phase [38]. The transition temperature is about 100 K for hole densities below 10^{20} cm^{-3} but decreases at higher concentrations [39]. In ferroelectric SnTe, the dielectric dipole moment arises from an offset of the cation and anion sublattices along the cubic ⟨111⟩ direction, combined with a shortening of the cubic body diagonal [21]. The ferroelectric distortion matches the displacement pattern (eigenvector) of the TO phonon at the zone center (Γ), and the transition has early been interpreted in terms of the soft-mode theory of ferroelectricity initially proposed by Cochran [25] and Pawley *et al.* [26].

In this study, the phonon density of states (DOS) of SnTe and PbTe were measured at a series of temperatures with INS. In addition, the atomic mean-square displacements were measured with neutron diffraction on both single-crystalline and powder samples. The combination of these measurements provides a detailed view of the phonon dynamics and anharmonicity. First-principles lattice dynamics and molecular dynamics simulations were performed and showed good agreement with the measured quantities in addition to reproducing the asymmetry of the first nearest-neighbor (1NN) peak in the radial distribution function reported in Refs. [27,28].

II. EXPERIMENTS

Single crystals of SnTe and PbTe were grown by a modified Bridgman technique and characterized with x-ray diffraction and transport measurements. Samples from the same growth were used for the measurements and characterization. For powder neutron diffraction and inelastic scattering phonon

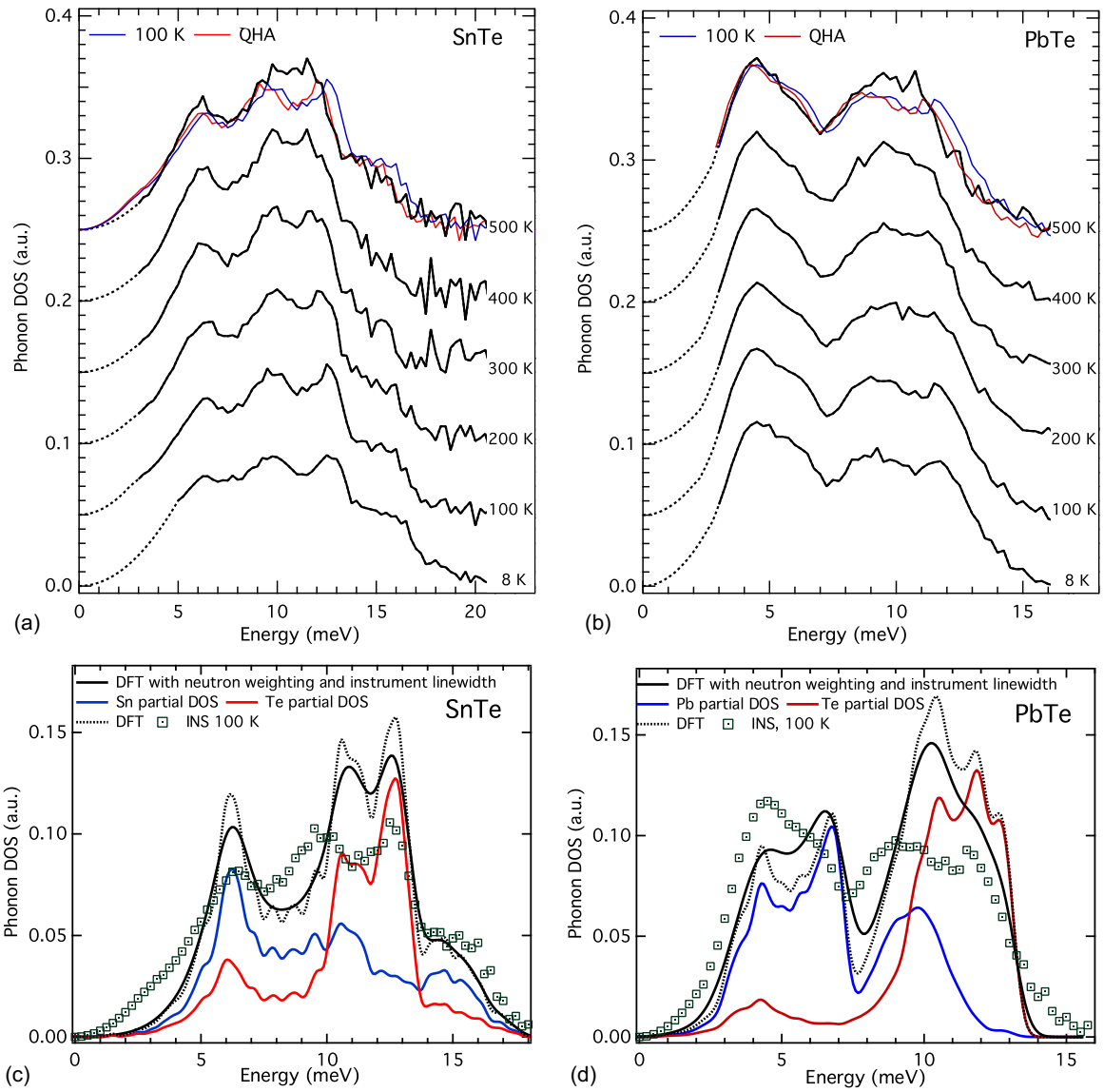

FIG. 1. (Color online) Phonon density of states of SnTe and PbTe. Generalized phonon DOS of (a) SnTe and (b) PbTe at several temperatures, obtained from powder inelastic neutron scattering on ARCS (incident energy $E_i = 30$ and 25 meV). The curve labeled quasiharmonic approximation (QHA) corresponds to data at 100 K, shifted according to the quasiharmonic approximation, with the measured volumes at 100 and 500 K and an average Grüneisen parameter $\gamma = 2$ from Ref. [44]. Panels (c) and (d) show the total and partial phonon DOS obtained from first-principles calculations. The results after applying neutron weighing and instrument resolution are compared with the neutron DOS at 100 K.

DOS measurements, some single crystals were ground into fine powders. The carrier concentration determined from Hall measurements was $n_h \simeq 6.5 \pm 1.5 \times 10^{20}$ h/cm^3 in SnTe crystals and $n_e \simeq 1.7 \times 10^{17}$ e/cm^3 in PbTe crystals. The low-temperature ferroelectric distortion of SnTe is very small [21], and we could not resolve any splitting of Bragg peaks with either powder or single-crystal neutron diffraction. However, the resistivity measurements on our SnTe crystals showed an anomaly characteristic of the ferroelectric transition at $T_C \simeq 42$ K [36]. This transition temperature is consistent with expectations for this carrier density, based on Raman measurements, transport characterization, and diffraction peak intensities [21,40]. On the other hand, PbTe at the present carrier concentration remains an incipient ferroelectric with an extrapolated $T_C \simeq -60$ K [21].

The phonon DOS measurements were performed on the powders with the wide angular-range chopper spectrometer (ARCS) time-of-flight neutron spectrometer at the Spallation Neutron Source (SNS) [41]. The samples were measured at $T = 8$, 100, 200, 300, 400, and 500 K, using an incident neutron energy of 30 or 25 meV for SnTe and PbTe, respectively. ARCS has an energy-dependent energy resolution that varies from about 4% at the elastic line to 1% at the highest energy transfer. The signal from the empty aluminum sample holder was measured in identical conditions and subtracted from the data. The time-of-flight data were reduced with MANTID [42] to produce the powder-averaged dynamical structure factor $S(Q,E)$ as a function of energy transfer E and momentum transfer magnitude Q. From this $S(Q,E)$, the generalized (neutron-weighted) phonon DOS was obtained by applying corrections for thermal occupation as well as multiphonon and multiple scatterings with an incoherent scattering approximation [43]. The results for the phonon DOS are shown in Fig. 1.

Powder and single-crystal neutron diffraction measurements were performed with POWGEN and TOPAZ at SNS and HB-3A at the High-Flux Isotope Reactor (HFIR). In the POWGEN powder diffraction measurements, two frames corresponding to bands of neutron wavelengths centered around 0.533 and 1.59 Å were used to cover a large range of momentum transfers. The powder was loaded in a vanadium can and mounted in either a closed-cycle refrigerator or a furnace for measurements from 100 to 450 K. For single-crystal diffraction measurements on TOPAZ and HB-3A, samples were cut into cubes about $2 \times 2 \times 2$ mm^3 and $3 \times 3 \times 3$ mm^3, respectively, with the corners rounded. After cutting and shaping, all samples were sealed in quartz tubes and annealed at 600 K for 3 days. On TOPAZ, the crystals were mounted in a cold nitrogen flow and measured using neutron wavelengths between 0.3 and 3.5 Å at 100, 200, 300, 350, 400, and 450 K. On HB-3A, the crystals were mounted in a high-temperature closed-cycle refrigerator and measured using neutron wavelengths of 1.003 Å at 5, 50, 100, 150, 200, 250, 300, and 450 K. The integrated peak intensities were analyzed with the software FULLPROF [45], and atomic mean-square displacements (MSDs) were obtained from the Rietveld refinements. Typical refinement factors at 300 K were listed in Table I. The results for MSD values as function of temperature are shown in Fig. 2. It should be noted that our SnTe crystals are in low-symmetry phase at $T < 42$ K.

TABLE I. Diffraction refinement parameters at 300 K.

	HB-3A				TOPAZ			
	SnTe		PbTe		SnTe		PbTe	
RF^2w	3.60		6.19		6.8		6.0	
RF	1.83		3.07		3.6		2.7	
χ^2	0.569		3.00		2.83		4.02	
$\langle u^2 \rangle$	Sn	Te	Pb	Te	Sn	Te	Pb	Te
(10^{-2} Å^2)	1.919	1.467	2.025	1.528	2.269	1.521	2.369	1.705

Single-crystal inelastic neutron scattering (INS) measurements were performed with the CNCS cold neutron time-of-flight spectrometer at the SNS [46] and the cold triple-axis spectrometer (CTAX) at HFIR. CNCS measurements were performed with incident energies $E_i = 12$ and 25 meV (the energy resolution at the elastic line is 0.5 meV) and at two different temperatures (50 and 300 K). The crystals

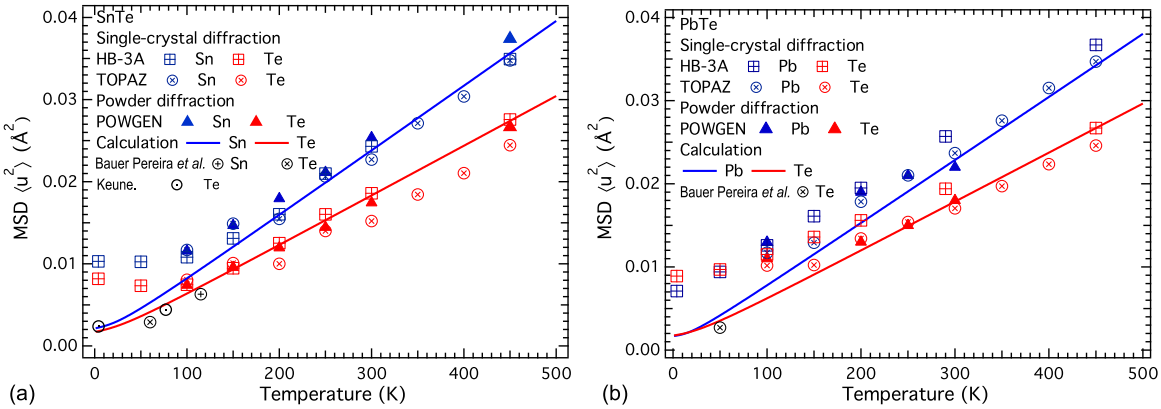

FIG. 2. (Color online) Mean-square atomic displacements for (a) SnTe and (b) PbTe, measured with neutron diffraction (markers) and calculated (lines) from the theoretical partial phonon DOS curves of Fig. 1. Open color markers correspond to MSD values measured with neutron single-crystal diffraction (HB-3A and TOPAZ), whereas filled color markers are values from powder diffraction (POWGEN). Black markers correspond to values in the literature. Blue lines and markers correspond to Sn or Pb, and red lines correspond to Te. The vibration amplitudes of the cations are systematically larger than those of Te anions.

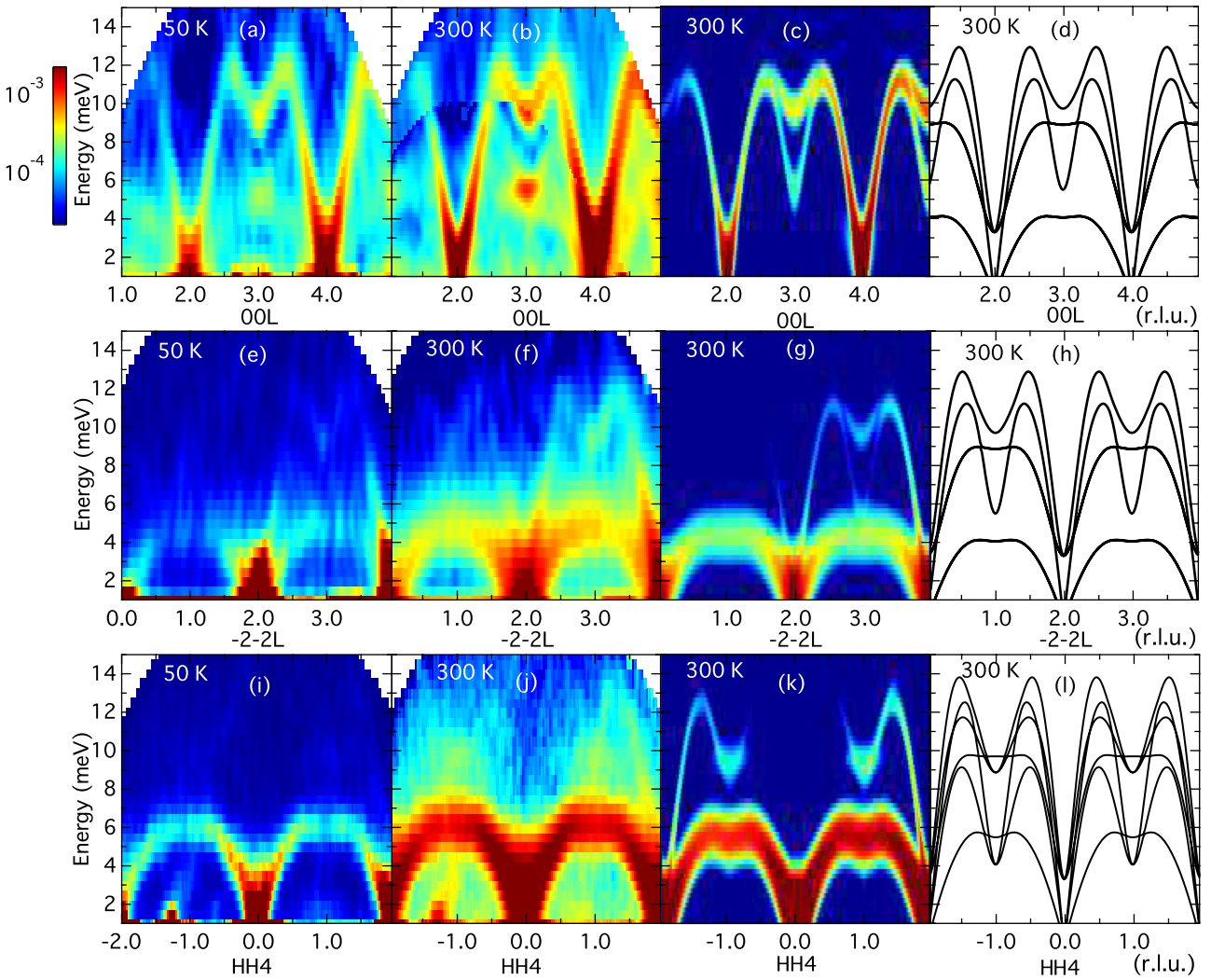

FIG. 3. (Color online) SnTe: slices of dynamical structure factor $S(Q,E)$ along the $[0,0,L]$ direction measured on CNCS at (a) 50 and (b) 300 K, compared with (c) first-principles simulations and (d) phonon dispersion. $S(Q,E)$ along the $[-2,-2,L]$ direction showing same phonon dispersion branches but stronger transverse acoustic phonons, owing to polarization factor $(\mathbf{Q}\cdot\epsilon_{ds})$ in Eq. (1), measured at (e) 50 and (f) 300 K, compared with (g) first-principles simulations and (h) phonon dispersion. $S(Q,E)$ along the $[H,H,4]$ direction measured on CNCS at (i) 50 and (j) 300 K, compared with (k) first-principles simulations and (l) phonon calculation. [Intensities are integrated over ± 0.1 r.l.u. (where r.l.u. represents reciprocal lattice unit) along the $[0,0,1]$ and $[1,\bar{1},0]$ directions and plotted on a logarithmic scale.]

were oriented with the $[\bar{1}10]$ axis vertical, and data were collected for multiple rotations around this direction over a wide range of angles. The data were subsequently combined to generate the four-dimensional scattering function $S(\mathbf{Q},E)$ using standard software [42,47] and then "sliced" along selected $\mathbf{Q}$ directions to produce two-dimensional views, some of which are shown in Fig. 3 for SnTe. Data from lower incident energy provides better resolution but limited $\mathbf{Q}$ and E coverage. Acoustic phonons of SnTe near the Γ point were measured with CTAX using a PG002 monochromator and analyzer with a constant final energy $E_f = 5.0$ meV and collimation settings of 48′-40′-40′-120′. The spectra for longitudinal acoustic phonons were refined to extract the phonon energy and linewidth by computing the convolution of the CTAX instrument resolution function with a Lorenzian function as implemented in the single mode approximation in the RESLIB package [48]. Figure 4 shows the results from fitting the constant-$\mathbf{Q}$ cuts from both CTAX and CNCS.

III. FIRST-PRINCIPLES SIMULATIONS

There has been considerable interest in calculating the phonon modes in SnTe and PbTe [50–52]. Although some of these calculations reproduced the soft TO phonon modes and the lattice instability at low temperatures, they offered only limited insight about the anharmonicity, except for a recent study by Lee *et al.* [14]. In order to capture the full extent of anharmonicity on the phonons at finite temperatures, *ab initio* Born-Oppenheimer MD simulations were performed at 100, 300, and 600 K with VASP [53–55]. Calculations used the generalized gradient approximation [Perdew-Burke-Ernzerhof (PBE)] and projector augmented-wave (PAW AM05) pseudopotentials with an energy cutoff of 300 meV. The MD

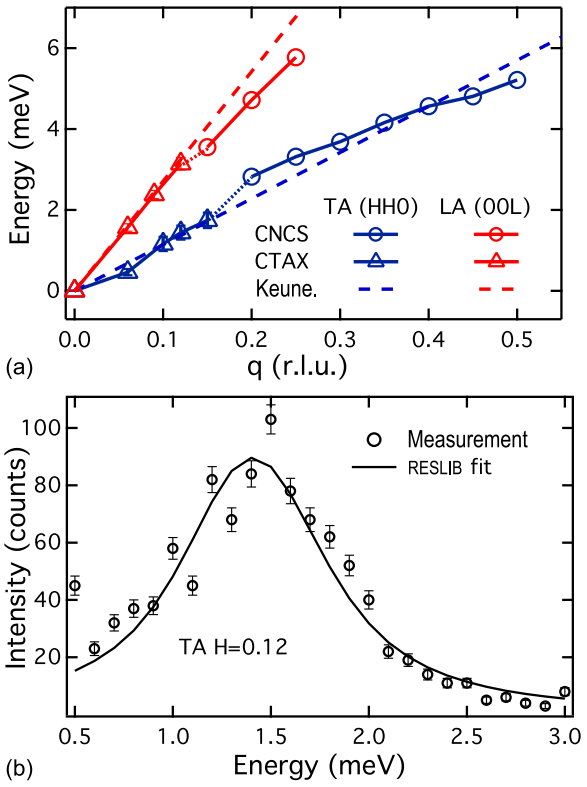

FIG. 4. (Color online) Longitudinal acoustic phonon dispersion relation and linewidth near the zone center, measured near 002 on CTAX and near 004 on CNCS along the (a) $HH0$ and $00L$ directions at 300 K. The error bars indicate the measured phonon linewidth after instrument resolution correction. The dashed lines show the results from sound velocity measurements [49]. The measurements are resolution limited for CNCS, and no resolution is shown. The RESLIB fit for the TA mode at $q = [0.12,0.12,0]$ is shown in (b).

simulations of a $3 \times 3 \times 3$ (216 atoms) supercell were first carried out with Γ-point-only Brillouin-zone integration for more than 20 ps after equilibration with a time step of 2 fs, and the temperature was controlled with a Nosé thermostat. Subsequently, 30 uncorrelated steps from the MD trajectories were recalculated with a $3 \times 3 \times 3$ electronic k-point grid. The convergence was tested against the size of the supercell, cutoff energy, simulation length, and cutoff distance of the force constants. The translational invariance was imposed. Harmonic, third-, and fourth-order anharmonic terms in interatomic force constants were obtained by fitting an effective anharmonic Hamiltonian to these atomic configurations and corresponding forces following the temperature-dependent effective potential (TDEP) methodology as developed by Hellman *et al.* [56]. The phonon DOS and dispersions were calculated using renormalized harmonic force constants at 300 K (from the TDEP procedure). The total and atom-projected (partial) phonon DOS computed for SnTe and PbTe using tetrahedron integration are shown in Figs. 1(a) and 1(b). The phonon dispersions of SnTe are shown in Fig. 3 (last column). First-principles frozen phonon calculations show that, at their respective relaxed lattice parameters, SnTe has a double-well potential with two minima offset from the rock-salt position, whereas PbTe shows a single minimum centered at the equilibrium configuration [36]. This is in good agreement with the experimental observation that stoichiometric SnTe is ferroelectric whereas PbTe is paraelectric down to 0 K, and thus SnTe is closer to the ferroelectric instability than PbTe. The TDEP method at the calculated temperatures yields stable phonons and reproduces the experimental observation of stabilization of the soft TO mode with increasing T.

In order to compare with the INS measurements, the dynamical structure factor was computed from the first-principles phonon dispersions and polarization vectors (ϵ_{ds}) as follows [57]:

$$S(\mathbf{Q},E) \propto \sum_s \sum_\tau \frac{1}{E_s} \left| \sum_d \frac{\bar{b}_d}{\sqrt{M_d}} e^{(-W_d + i\mathbf{Q}\cdot\mathbf{r}_d)} (\mathbf{Q}\cdot\epsilon_{ds}) \right|^2 \times \langle n_s + 1 \rangle \delta(E - E_s) \delta(\mathbf{Q} - \mathbf{q} - \tau), \quad (1)$$

where s, τ, and d denote the branch index, reciprocal lattice vector, and atom index in the unit cell, respectively, and $\bar{b}_d$, $\mathbf{r}_d$, and M_d are the coherent neutron scattering length, position, and atomic mass for atom d. The Debye-Waller factor W_d was calculated assuming the MSDs are isotropic and using their values from the simulation as described earlier. The result was convoluted with a four-dimensional Gaussian instrument resolution function for CNCS $R(\mathbf{Q},E)$. A constant $\mathbf{Q}$ resolution of comparable width as the bin sizes of $S(\mathbf{Q},E)$ integration and a known energy-dependent energy resolution were used [46]. The results are in good agreement with the INS measurement as can be seen in Fig. 3, validating the finite-temperature phonon dispersion calculations.

IV. LATTICE DYNAMICS

Phonon dispersions of SnTe were measured at 100 K by Cowley *et al.* [50], but that study did not investigate the temperature dependence. Although Pawley *et al.* reported the temperature dependence of the TO mode from 6 to 300 K, their sample remained cubic at all temperatures, probably as a result of a high hole concentration [26]. The partial phonon DOS of Sn and Te were previously measured in rock-salt SnTe at 60 K using nuclear-resonant inelastic x-ray scattering, and it was found that the phonons are softer than similar materials in the rhombohedral phase [58]. In addition, a lattice dynamics study of SnTe using Mössbauer spectroscopy suggested the existence of low-temperature anharmonicity [59]. Our more detailed measurements of the temperature-dependent phonon dispersions and DOS provide further information about the phonon dynamics and anharmonicity and enable us to clarify the origin of asymmetric PDF/RDF peaks observed in diffraction experiments.

Generalized phonon DOS curves from inelastic neutron scattering are "neutron weighted" because phonon scattering by the different elements occurs with different efficiencies, proportional to their total neutron scattering cross section divided by atomic mass σ_{scat}/M. For comparison with experimental results, the TDEP calculated phonon partial DOS curves of Sn/Pb and Te were multiplied by σ_{scat}/M and summed to give neutron-weighted DOS curves. The result was then convoluted with the energy-dependent instrument resolution function of ARCS to produce an approximate experimental phonon DOS with neutron weighting as shown in Fig. 1.

We find a fair agreement between this neutron-weighted phonon DOS curve, calculated in the renormalized harmonic approximation with TDEP and the generalized phonon DOS from powder INS for SnTe and PbTe as can be seen in Fig. 1. The neutron-weighted phonon DOS agrees well with previous nuclear inelastic scattering measurement of Sn and Te at 115 and 60 K, respectively [58]. However, there are a few differences between INS and calculation. The experimental DOS for SnTe shows a higher intensity near 3 to 4 meV at $T = 100$ K, which subsides at higher temperatures. This is in agreement with the very soft nature of the zone-center TO phonon mode at 100 K as a precursor to the ferroelectric phase transition. The experimental DOS for PbTe shows a lesser enhancement at low energy, consistent with the incipient character of the ferroelectric transition in this material ($T_C < 0$). In both materials, there are also some differences in the midenergy region between 7 and 11 meV with the measured DOS showing softer and broader phonon modes. According to calculated phonon dispersion relations (Fig. 3) and mode eigenvectors, a large contribution to DOS in this range arises from transverse-optical phonons. This discrepancy between the measured DOS and the harmonic calculations is thus consistent with the anharmonicity of the TO branches. This is consistent with the previous results that the low-energy phonons are confined to the zone center and have small influence on the phonon DOS. Using the simulated partial phonon DOS, it is possible to correct the neutron weighting from the measured generalized phonon DOS. After performing this correction, we find that the average phonon energies in the deweighted DOS at 100 K (Fig. 1) are 9.9 and 8.2 meV for SnTe and PbTe, respectively. The Debye temperatures (θ_D), calculated from the average phonon energy ($\langle E \rangle$) using $k_B\theta_D = \frac{4}{3}\langle E \rangle$, are 115 and 95 K, respectively.

The temperature dependence of the phonon DOS provides insight into the thermal effects on the vibrational energies in the lattice. All DOS curves show three main peaks, which correspond to the flat portions at the top of phonon dispersions (van Hove singularities). Whereas the lowest peak between 4 and 7 meV is dominated by the top of the transverse-acoustic (TA) branches, the other two are mixtures of longitudinal acoustic (LA), TO, and longitudinal optical branches. For both materials, the peak at intermediate energies (around 9 meV at 100 K) slightly stiffens with increasing T, whereas the higher-energy peak (around 12 meV at 100 K) significantly softens, leading to these two peaks merging. On the other hand, the low-energy TA peak appears almost unaffected by temperature.

Using an average Grüneisen parameter of 2.0 as calculated from the third-order interatomic force constants using the TDEP method as described in Ref. [60] and in agreement with a thermodynamical estimate [44] and using the thermal expansion results from neutron diffraction, it is possible to simulate the effect of lattice dilation with the QHA. The results for both SnTe and PbTe, shown as the red line in Fig. 1, are quite different from the high-temperature measurement, indicating a large amount of anharmonicity, especially for the higher-energy optical phonons.

We note that for both SnTe and PbTe, there is a spectral separation between the metal and the tellurium partial phonon DOS. Although this is expected for PbTe because of its large cation/anion mass ratio ($M_{Pb}/M_{Te} = 1.62$), it is unexpected for SnTe since Sn is slightly lighter than Te ($M_{Sn}/M_{Te} = 0.93$). However, this behavior is understood by inspecting the magnitude of the on-site force constants, which are significantly smaller for the cations than for the anions. This trend is already observed in harmonic-level calculations of the force constants and remains valid in finite-temperature TDEP calculations. For example, the on-site force constant on Te (3.0 eV/Å for the harmonic model and 2.7 eV/Å for TDEP at 300 K) is larger than the one on Sn (2.2 eV/Å for the harmonic model and 2.0 eV/Å for TDEP at 300 K). As a result, Te contributes more to the higher-energy portion of the DOS than Sn. This may be understood from the bonding states resulting primarily from extended Te p orbitals pointed along $\langle 100 \rangle$ [14].

Further examination of force constants from TDEP provides important insight about the bonding in these materials. Our calculations find the largest harmonic force constants between fourth nearest-neighbor (4NN) atoms in SnTe, which correspond to second neighbors along $\langle 100 \rangle$ directions (Sn-Sn and Te-Te: both 0.56 eV/Å^2 at 300 K), even larger than the 1NN Sn-Te term, also along $\langle 100 \rangle$ (0.36 eV/Å^2 at 300 K). The trend is similar in PbTe (Pb-Pb 4NN: 0.49 eV/Å^2, Te-Te 4NN: 0.52 eV/Å^2, and Pb-Te 1NN: 0.40 eV/Å^2). Even for third-order force constants, the terms involving 4NN atoms are larger than all others, except for the 1NN bonds. In all cases, the harmonic and anharmonic force constants are strongly anisotropic with longest-range interactions along the $\langle 100 \rangle$ directions. These results are in line with the recent analysis of force constants by Lee *et al.* in terms of resonant bonding in PbTe and SnTe [14].

From our SnTe measurements on CTAX, phonon scattering rates were extracted from which the contribution of acoustic phonons to the lattice thermal conductivity κ_{lat} could be estimated. The contribution of a given phonon mode $(\mathbf{q}, j)$ to the total κ_{lat} is as follows: $\kappa_{latt,\mathbf{q},j} = \frac{1}{3} c_{\mathbf{q},j} v^2_{\mathbf{q},j} \tau_{\mathbf{q},j}$, where $c_{\mathbf{q},j}$ is the mode heat capacity, $v_{\mathbf{q},j} = |\partial\omega_{\mathbf{q},j}/\partial\mathbf{q}|$ is the mode group velocity, and $\tau_{\mathbf{q},j} = \hbar/(2\Gamma_{\mathbf{q},j})$ is the mode lifetime, determined from the measured mode linewidth $2\Gamma_{\mathbf{q},j}$. From neutron measurements of SnTe, the group velocities are approximately 4.00×10^3 and 1.25×10^3 m/s for the LA mode along $[0,0,L]$ and for the TA mode along $[H,H,0]$, respectively, according to the dispersion slopes shown in Fig. 4. It should be noted that the sound velocities in SnTe depend on the carrier concentration. Ultrasound measurements on a sample with a hole concentration of $n_h = 4.5 \times 10^{20}$ h/cm^3, close to the value in our sample, yield velocities of 4120 m/s for the LA mode along $[0,0,L]$ and 1220 m/s for the TA mode along $[H,H,0]$ polarized in the $[0,0,L]$ direction [49]. The phonon linewidths with instrument contribution subtracted at 0.1 r.l.u. from the zone center are 0.31 and 0.35 meV for the LA and TA modes, respectively. These values were obtained from the refinement as mentioned earlier. Using the measured linewidths, the average group velocity of the three modes and the total lattice heat capacity of SnTe, the estimated contribution from acoustic modes is 2.8 W m^{-1} K^{-1} at 300 K. This estimate is larger than the value determined by subtracting the electronic component from the total thermal conductivity measurement [2 W m^{-1} K^{-1}], especially considering that

optical modes are expected to also contribute about 20% of the lattice conductivity [13]. The overestimation is likely associated with our simple extrapolation of linear acoustic dispersions to the entire Brillouin zone.

V. ATOMIC DISTRIBUTIONS

In Fig. 2, we compare the atomic mean-square displacements obtained from diffraction experiments with three different instruments (TOPAZ and HB-3A for single crystals and POWGEN for powders). The results from these different measurements agree well overall. The single-crystal diffraction measurements provided more accurate intensities of the Bragg peaks, especially for the odd-order peaks in SnTe, which are especially weak due to the small contrast between Sn and Te neutron scattering lengths. As a result, for SnTe we expect more reliable refinement of the MSD with a single crystal than powder diffraction. The contrast between Pb and Te is stronger, and this was less an issue in PbTe powder measurements.

In the harmonic approximation, the MSD for each crystallographic site and species solely depends on its partial phonon DOS $g(\omega)$ and atomic mass M and can be calculated with temperature-dependent phonon occupations [57],

$$\langle u^2_{\text{har}} \rangle = \frac{3\hbar}{2M} \int \frac{1}{\omega} \coth\left(\frac{\hbar\omega}{2k_B T}\right) g(\omega) d\omega. \quad (2)$$

In Fig. 2, we compare the measured MSD in PbTe and SnTe (markers) with the expected value in the harmonic approximation based on the partial phonon DOS calculated from first principles (lines). The results are similar to those at low temperatures in the literature, also calculated from partial phonon DOS [58] for Sn and Te and from Mössbauer [59] for Te, although a direct comparison is not warranted since carrier concentrations were not reported for samples used in those studies. The calculated and measured MSD are in good agreement above 100 K in both systems. In particular, we do not see any constant offset at high temperatures, which rules out the presence of static displacements. We note that both anions and cations show MSDs that are linear in T at high temperatures with a larger slope for cations. The larger cation MSD was noted in Ref. [58], but no clear origin for the effect was found. Our detailed DFT simulations actually reveal that these large MSD values for cations arise from the weaker on-site force constants for cations, in good agreement with prior DFT investigations of the bonding and phonons in these materials [11–14,37]. This is in agreement with the equation above since the weaker cation bonding leads to their softer partial phonon DOS discussed above. On the other hand, below 100 K, the MSDs from diffraction experiments significantly exceed the harmonic prediction (Fig. 2) for both SnTe and PbTe. This behavior is expected because some phonon modes, especially the TO modes near the zone center, have a strongly anharmonic potential-energy curve with a flat bottom (or a shallow double well in the case of SnTe), resulting in larger zero-point motion than expected for harmonic oscillators. Since the strongly anharmonic portion of the soft TO mode is confined to a small reciprocal volume around the zone center, the soft mode only contributes a small spectral weight in the phonon DOS, but it can still provide a large MSD. Although some residual contribution from the Rietveld refinement procedure cannot be entirely ruled out, we note that there is no systematic offset between the refined ADPs at high temperatures and the values computed from Eq. (2). At high temperatures, the good agreement between the measured MSDs and the harmonic model is expected since the entire phonon spectrum is thermally populated and most of these modes behave harmonically. On the other hand, the steep walls of the TO potential lead to a reduced relative MSD contribution from the soft mode at high temperatures, especially as it is strongly renormalized [36]. Thus, the proposal that atoms would occupy off-centered positions increasingly deviating from their average crystallographic sites as T increases [27–29] is not supported by our data. Instead, we find that the large MSDs, increasing linearly at high T, are predominantly a reflection of large-amplitude thermal vibrations in these softly bonded materials, in agreement with first-principles simulations. We also note that our results for PbTe are in good agreement with those of Ref. [33] for PbS, adjusted for the heavier overall mass of PbTe.

To understand the asymmetric peaks in the PDFs and RDFs reported in the literature [9,27,29], we performed several types of molecular dynamics simulations. Because it is straightforward to convert between the PDF and the RDF with different normalizations, to illustrate the peak asymmetry better, the RDF was used for discussion here. First, the RDF was directly calculated from the first-principles molecular dynamics trajectories (the same potentials and supercell as described earlier, $3 \times 3 \times 3$ electronic k-point grid, 10 ps at a 2-fs time step, and $T = 100$, 300, 600 K). Results are shown as solid lines in Figs. 5(a) and 5(c) for SnTe and PbTe, respectively. For both SnTe and PbTe, these first-principles MD RDFs reproduce the asymmetry of the peaks observed experimentally from x-ray diffraction ("total scattering") [27,28] and reproduced in previous *ab initio* MD simulations [11] and classical MD simulations based on anharmonic interatomic potentials [30]. The distortion of the peaks is obvious for $T \geqslant 300$ K and can be quantified in terms of the peak skewness γ, which is defined as the third standardized moment $\gamma = \mu_3/\sigma^3$ in which μ_3 is the third central moment and σ is the standard deviation. The skewness of the 1NN peak is $\gamma = 0.413$ and 0.379 for SnTe and PbTe at 300 K, respectively. The skewness takes similar values at 600 K, but it is much smaller at 100 K (SnTe: 0.224; PbTe: 0.180). The average MSD of SnTe at 300 K, estimated by the width of the first nearest-neighbor peak in RDF $\langle u^2 \rangle = 0.022$ Å^2, is in good agreement with our diffraction measurements.

In order to evaluate the role of anharmonicity in the atomic potential, classical MD simulations on a same supercell were performed with effective harmonic force constants fitted to the *ab initio* molecular dynamics (AIMD) trajectories using the TDEP method described earlier. Such renormalized harmonic force constants were obtained for each AIMD temperature. Because of the low computational cost, the classical MD was performed for 200 ps at a 2-fs time step. We note that the resulting T-dependent renormalized harmonic potential was similar whether fits also included third- and fourth-order force constants or only the harmonic components. Harmonic RDFs were then calculated from the resulting harmonic MD trajectories. Strikingly, these harmonic RDFs

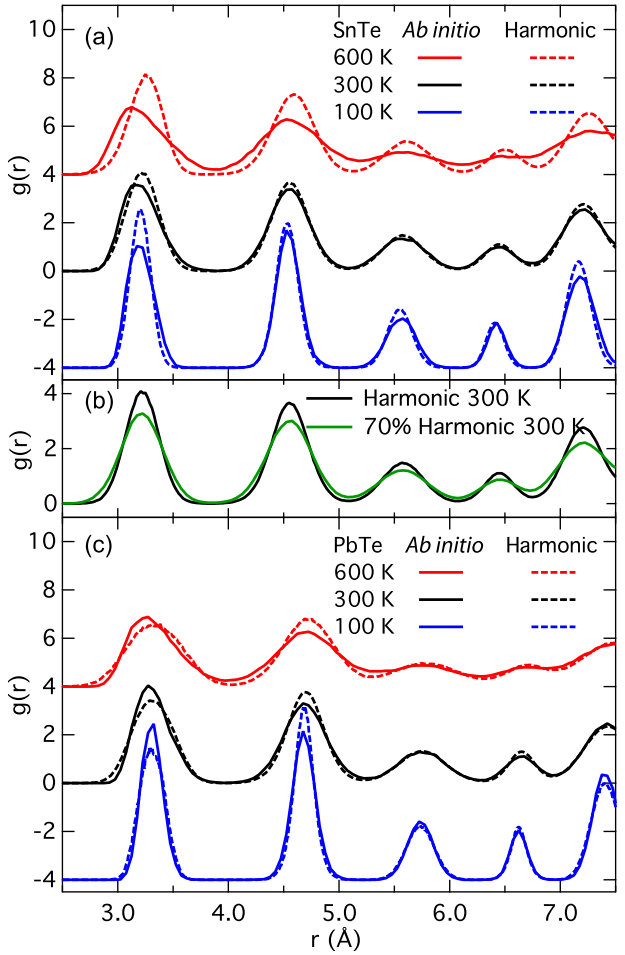

FIG. 5. (Color online) Radial distribution functions of (a) SnTe and (c) PbTe calculated from first-principles molecular dynamics and harmonic classical molecular dynamics (using effective harmonic force constants extracted from the former). Note that full anharmonic calculation results in asymmetric peaks, especially for the 1NN bond, whereas the harmonic model shows symmetric peaks. In addition, softening the harmonic force constants by 30% does not induce asymmetry, as shown by the results for SnTe in (b).

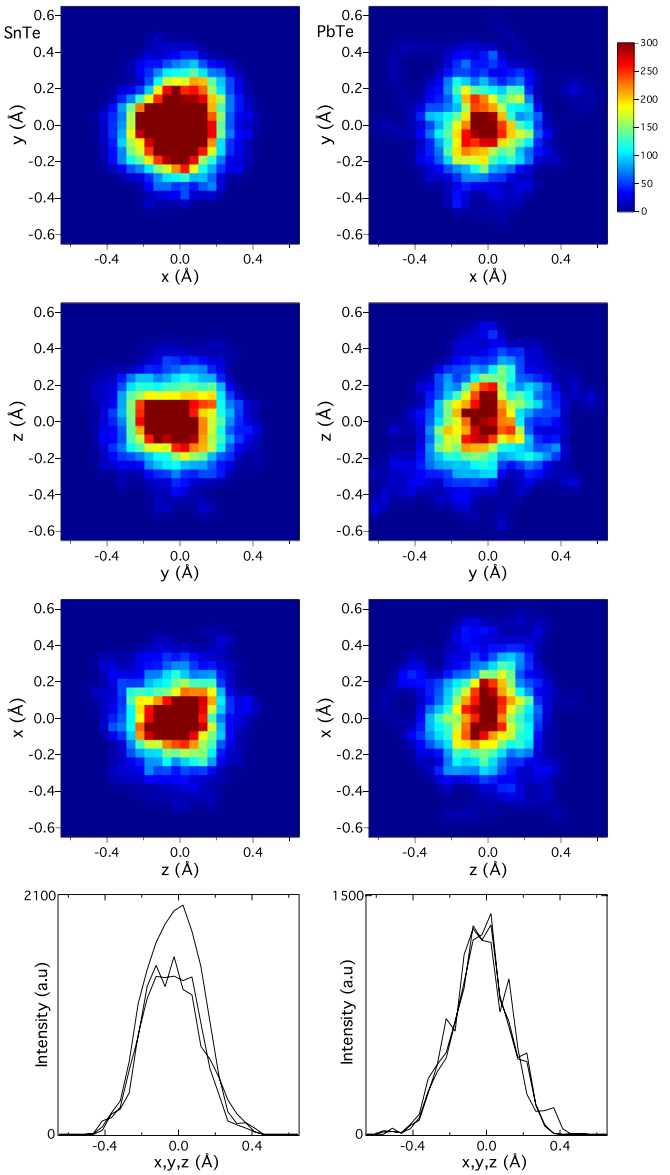

FIG. 6. (Color online) The probability distribution functions of the Sn/Pb atom in SnTe/PbTe, calculated from first-principles molecular dynamics at 300 K, show no sign of off centering. The origin is the average crystallographic position. The integration range along the axis perpendicular to the visualized plane is ±0.1 Å. The color scale is linear. For one-dimensional cuts, the integration ranges along the two integrated axes are both ±0.1 Å.

show almost symmetric peaks at all temperatures [dashed curves in Figs. 5(a) and 5(c)]. The skewness of the 1NN peaks in the RDF at 300 K is −0.002 and 0.053 for SnTe and PbTe, respectively, close to zero within the statistical uncertainty. This is a strong confirmation that the asymmetry in the RDF arises from the anharmonicity in the potential-energy surface of these materials. We note that the widths of the peaks in harmonic RDFs are almost the same as in the full anharmonic AIMD calculations. In addition, a harmonic classical MD for SnTe with its harmonic force constants reduced by 30% also resulted in an RDF with symmetric peaks as illustrated in Fig. 5(b). This indicates that weak force constants alone are not sufficient to induce asymmetry in the RDF and that anharmonicity is needed to produce the effect. Furthermore, we investigated the nuclear probability density function of Sn or Pb from the first-principles molecular dynamics trajectory. The results, shown in Fig. 6, confirm the absence of atomic off centerings in AIMD runs of a couple picoseconds, in agreement with prior simulations [11].

The asymmetry (skewness) of the 1NN peaks in the first-principles PDF of SnTe and PbTe are similar with the former being slightly larger. Their temperature dependence is also similar. On the other hand, we have previously shown that the zone-center TO phonon spectral functions of SnTe and PbTe are different. The TO mode spectral function in SnTe does not exhibit the double peak present in PbTe [36]. This leads to the conclusion that the asymmetry of the 1NN PDF peak probes anharmonicity differently than the phonon spectral function. Indeed, we have found that the harmonic, cubic, and quartic interatomic force constants in SnTe and PbTe have very similar values (similar bonding and

anharmonicity), explaining the similar RDFs [36]. On the other hand, the phonon spectral functions computed from the phonon self-energy showed that the anomalous line shape of the zone-center TO mode in PbTe results from an enhancement of the imaginary part of the self-energy, owing to the opening of a large phase space for three-phonon interactions [36]. We point out that asymmetry in the PDF peaks is a good indication of anharmonic interatomic potentials and could be used to screen materials for strong anharmonicity.

VI. CONCLUSION

The anharmonic lattice dynamics of rock-salt thermoelectric materials SnTe and PbTe were investigated with neutron diffraction, inelastic neutron scattering, and first-principles calculations. The atomic mean-square displacements were derived from the diffraction data and agree well with the values predicted from the partial phonon DOS above 100 K, indicating that there are no atomic off centerings at these temperatures. This conclusion is confirmed with *ab initio* molecular dynamics simulations, which show no off centering on a time scale of a few picoseconds. Radial distribution functions were calculated from molecular dynamics simulations, both at the level of PAW-PBE *ab initio* MD and using effective harmonic force constants derived from the high-temperature AIMD. The results indicate that the asymmetry of the peaks in the radial distribution function, in particular for the 1NN bond, can be explained by large-amplitude anharmonic thermal vibrations in atoms (i.e., anharmonic phonons).

ACKNOWLEDGMENTS

Neutron scattering work by O.D. was supported by the U.S. Department of Energy, Office of Science, Basic Energy Sciences, Materials Sciences and Engineering Division, through the Office of Science Early Career Research Program. Neutron scattering work by C.W.L. and J.M. was supported by the US Department of Energy, Office of Science, Basic Energy Sciences, as part of the S3TEC Energy Frontier Research Center, DOE Grant No. DE-SC0001299. Sample synthesis (A.F.M.) was supported by the U.S. Department of Energy, Office of Basic Energy Sciences, Materials Sciences and Engineering Division. Modeling of neutron data (C.W.L., O.D.) was developed as part of CAMM, funded by the U.S. Department of Energy, Basic Energy Sciences, Materials Sciences and Engineering Division. The use of Oak Ridge National Laboratory's Spallation Neutron Source and High Flux Isotope Reactor was sponsored by the Scientific User Facilities Division, Office of Basic Energy Sciences, U.S. DOE. This research used resources of the National Energy Research Scientific Computing Center, which is supported by the Office of Science of the U.S. DOE. O.G. thanks the Lujan Neutron Scattering Center at LANSCE, which was funded by the U.S. DOE Office of Science, Basic Energy Sciences. Los Alamos National Laboratory is operated by Los Alamos National Security LLC under DOE Contract No. DE-AC52-06NA25396. We thank O. Hellman for providing the TDEP software used in the calculation and B. C. Chakoumakos for helpful discussions.

[1] G. J. Snyder and E. S. Toberer, Nature Mater. **7**, 105 (2008).
[2] Y. Pei, X. Shi, A. LaLonde, H. Wang, L. Chen, and G. J. Snyder, Nature Mater. **473**, 66 (2011).
[3] K. Biswas, J. He, I. D. Blum, C.-I. Wu, T. P. Hogan, D. N. Seidman, V. P. Dravid, and M. G. Kanatzidis, Nature Mater. **489**, 414 (2012).
[4] D. Parker, X. Chen, and D. J. Singh, Phys. Rev. Lett. **110**, 146601 (2013).
[5] L. Xu, H.-Q. Wang, and J.-C. Zheng, J. Electron. Mater. **40**, 641 (2011).
[6] G. A. Akhmedova and D. S. Abdinov, Inorg. Mater. (USSR) **45**, 854 (2009).
[7] Q. Zhang, B. Liao, Y. Lan, K. Lukas, W. Liu, K. Esfarjani, C. Opeil, D. Broido, G. Chen, and Z. Ren, Proc. Natl. Acad. Sci. USA **110**, 13261 (2013).
[8] O. Delaire, J. Ma, K. Marty, A. F. May, M. A. McGuire, M.-H. Du, D. J. Singh, A. Podlesnyak, G. Ehlers, M. D. Lumsden, and B. C. Sales, Nature Mater. **10**, 614 (2011).
[9] K. M. O. Jensen, E. S. Božin, C. D. Malliakas, M. B. Stone, M. D. Lumsden, M. G. Kanatzidis, S. M. Shapiro, and S. J. L. Billinge, Phys. Rev. B **86**, 085313 (2012).
[10] J. An, A. Subedi, and D. J. Singh, Solid State Commun. **148**, 417 (2008).
[11] Y. Zhang, X. Ke, P. R. C. Kent, J. Yang, and C. Chen, Phys. Rev. Lett. **107**, 175503 (2011).
[12] T. Shiga, J. Shiomi, J. Ma, O. Delaire, T. Radzynski, A. Lusakowski, K. Esfarjani, and G. Chen, Phys. Rev. B **85**, 155203 (2012).
[13] Z. Tian, J. Garg, K. Esfarjani, T. Shiga, J. Shiomi, and G. Chen, Phys. Rev. B **85**, 184303 (2012).
[14] S. Lee, K. Esfarjani, T. Luo, J. Zhou, Z. Tian, and G. Chen, Nat. Commun. **5**, 3525 (2014).
[15] G. Lucovsky and R. M. White, Phys. Rev. B **8**, 660 (1973).
[16] P. B. Littlewood, J. Phys. C: Solid State Phys. **13**, 4855 (1980).
[17] P. B. Littlewood, J. Phys. C: Solid State Phys. **13**, 4875 (1980).
[18] A. Bussmann-Holder, H. Bilz, and P. Vogl, *Electronic and Dynamical Properties of IV-VI Compounds*, Springer Tracts in Modern Physics, Vol. 99 (Springer, Berlin, 1983), pp. 51–93.
[19] K. M. Rabe and J. D. Joannopoulos, Phys. Rev. B **32**, 2302 (1985).
[20] H. A. Alperin, S. J. Pickart, J. J. Rhyne, and V. J. Minkiewicz, Phys. Lett. A **40**, 295 (1972).
[21] W. Jantsch, *Dynamical Properties of IV-VI Compounds*, Springer Tracts in Modern Physics, Vol. 99 (Springer-Verlag, Berlin, 1983), pp. 1–48.
[22] P. Brüesch, *Phonons: Theory and Experiments* (Springer-Verlag, Berlin, 1982).
[23] G. P. Srivastava, *The Physics of Phonons* (Taylor and Francis, New York, 1990).
[24] B. Fultz, Progr. Mater. Sci. **55**, 247 (2010).
[25] W. Cochran, Adv. Phys. **9**, 387 (1960).
[26] G. S. Pawley, W. Cochran, R. A. Cowley, and G. Dolling, Phys. Rev. Lett. **17**, 753 (1966).

[27] E. S. Božin, C. D. Malliakas, P. Souvatzis, T. Proffen, N. A. Spaldin, M. G. Kanatzidis, and S. J. L. Billinge, Science **330**, 1660 (2010).
[28] K. R. Knox, E. S. Božin, C. D. Malliakas, M. G. Kanatzidis, and S. J. L. Billinge, Phys. Rev. B **89**, 014102 (2014).
[29] S. Kastbjerg, N. Bindzus, M. Søndergaard, S. Johnsen, N. Lock, M. Christensen, M. Takata, M. A. Spackman, and B. B. Iversen, Adv. Funct. Mater. **23**, 5477 (2013).
[30] T. Shiga, T. Murakami, T. Hori, O. Delaire, and J. Shiomi, Appl. Phys. Express **7**, 041801 (2014).
[31] F. Bridges, T. Keiber, S. Medling, and B. C. Sales, Phys. Status Solidi C **10**, 236 (2013).
[32] T. Keiber, F. Bridges, and B. C. Sales, Phys. Rev. Lett. **111**, 095504 (2013).
[33] K. S. Knight, J. Phys.: Condens. Matter **26**, 385403 (2014).
[34] S. W. Lovesey, *Theory of Neutron Scattering from Condensed Matter* (Clarendon, Oxford, 1984), Vol. 1.
[35] H. Burkhard, G. Bauer, and A. Lopez-Otero, J. Opt. Soc. Am. **67**, 943 (1977).
[36] C. W. Li, O. Hellman, J. Ma, A. F. May, H. B. Cao, X. Chen, A. D. Christianson, G. Ehlers, D. J. Singh, B. C. Sales, and O. Delaire, Phys. Rev. Lett. **112**, 175501 (2014).
[37] Y. Chen, X. Ai, and C. A. Marianetti, Phys. Rev. Lett. **113**, 105501 (2014).
[38] E. I. Rogacheva, G. V. Gorne, N. K. Zhigareva, and A. B. Ivanova, Inorg. Mater. **27**, 194 (1991).
[39] M. Iizumi, Y. Hamaguchi, K. F. Komatsubara, and Y. Kato, J. Phys. Soc. Jpn. **38**, 443 (1975).
[40] K. L. I. Kobayashi, Y. Kato, Y. Katayama, and K. F. Komatsubara, Phys. Rev. Lett. **37**, 772 (1976).
[41] D. L. Abernathy, M. B. Stone, M. J. Loguillo, M. S. Lucas, O. Delaire, X. Tang, J. Y. Y. Lin, and B. Fultz, Rev. Sci. Instrum. **83**, 015114 (2012).
[42] J. Taylor *et al.*, *Bulletin of the American Physical Society,* Vol. 57 (APS, 2012).
[43] M. Kresch, O. Delaire, R. Stevens, J. Y. Y. Lin, and B. Fultz, Phys. Rev. B **75**, 104301 (2007).
[44] T. F. Smith, J. A. Birch, and J. G. Collins, J. Phys. C: Solid State Phys. **9**, 4375 (1976).
[45] J. Rodríguez-Carvajal, Phys. B **192**, 55 (1993).
[46] G. Ehlers, A. A. Podlesnyak, J. L. Niedziela, E. B. Iverson, and P. E. Sokol, Rev. Sci. Instrum. **82**, 085108 (2011).
[47] T. G. Perring, R. A. Ewings, and J. V. H. Duijn, http://horace.isis.rl.ac.uk.
[48] http://www.neutron.ethz.ch/research/resources/reslib.
[49] T. Seddon, S. C. Gupta, and G. A. Saunders, Solid State Commun. **20**, 69 (1976).
[50] E. R. Cowley, J. K. Darby, and G. S. Pawley, J. Phy. C: Solid State Phys. **2**, 1916 (1969).
[51] N. Gillis, Phys. Rev. Lett. **22**, 1251 (1969).
[52] D. Strauch and R. Becher, J. Phys. C: Solid State Phys. **20**, 1641 (1987).
[53] G. Kresse and J. Furthmüller, Comput. Mater. Sci. **6**, 15 (1996).
[54] G. Kresse and J. J. Hafner, Phys. Rev. B **47**, 558 (1993).
[55] G. Kresse and J. Furthmüller, Phys. Rev. B **54**, 11169 (1996).
[56] O. Hellman, P. Steneteg, I. A. Abrikosov, and S. I. Simak, Phys. Rev. B **87**, 104111 (2013).
[57] G. Squires, *Introduction to the Theory of Thermal Neutron Scattering* (Cambridge University Press, Cambridge, UK, 1978).
[58] P. Bauer Pereira, I. Sergueev, S. Gorsse, J. Dadda, E. Müller, and R. P. Hermann, Phys. Status Solidi B **250**, 1300 (2013).
[59] W. Keune, Phys. Rev. B **10**, 5057 (1974).
[60] O. Hellman and I. A. Abrikosov, Phys. Rev. B **88**, 144301 (2013).